

Modelling the Genesis of Sand-Starved Dunes in Steady Currents.

Gaetano Porcile¹, Johan H. Damveld², Pieter C. Roos², Paolo Blondeaux¹, and Marco Colombini¹

¹University of Genoa

²University of Twente

November 21, 2022

Abstract

The formation of fluvial dunes has been usually investigated assuming an infinite availability of the mobile sediment. Field observations and laboratory experiments nevertheless indicate that the volume of sediment available for transport affects their morphology. Here we undertake a stability analysis showing the formation of small amplitude sand dunes in steady currents accounting for the effects of sediment starvation on their formative mechanisms and compare it against laboratory experiments and an application of a fully numerical commercial model of finite amplitude dunes, thus enabling an improved understanding of the genesis of starved fluvial dunes. Both small and finite amplitude dunes are shown to be affected by sediment starvation. As their growth progressively exposes a motionless substratum, both models predict the lengthening of starved dunes with increasing irregularity in their spacing. These findings conform with the outcome of physical experiments performed in a laboratory flume and existing measurements of starved fluvial dunes in the field.

1 Modelling the Genesis of Sand-Starved Dunes in Steady Currents

2 Gaetano Porcile ¹, Johan H. Damveld ², Pieter C. Roos ², Paolo Blondeaux ³,
3 Marco Colombini ³

4 ¹ Coastal and Continental Morphodynamics Laboratory, University of Normandy, 24 rue
5 des Tilleuls, 14000 Caen, France

6 ² Water Engineering and Management, University of Twente, PO Box 217, 7500 AE
7 Enschede, the Netherlands

8 ³ Department of Civil, Chemical and Environmental Engineering, University of Genoa,
9 16145, Via Montallegro 1 Genoa, Italy

10 Abstract

11 The formation of fluvial dunes has been usually investigated assuming an infinite availability of
12 the mobile sediment. Field observations and laboratory experiments nevertheless indicate that
13 the volume of sediment available for transport affects their morphology. Here we undertake a
14 stability analysis showing the formation of sand dunes in steady currents accounting for the
15 effects of sediment starvation on their formative mechanisms and compare it against laboratory
16 experiments and an application of a fully numerical commercial model of finite amplitude dunes,
17 thus enabling an improved understanding of the genesis of starved fluvial dunes. Both small
18 and finite amplitude dunes are shown to be affected by sediment starvation. As their growth
19 progressively exposes a motionless substratum, both models predict the lengthening of starved
20 dunes with increasing irregularity in their spacing. These findings conform with the outcome
21 of physical experiments performed earlier in a laboratory flume and existing measurements of
22 starved fluvial dunes in the field.

23 Plain Language Summary

24 The formation of fluvial dunes has been usually investigated assuming an infinite availability of
25 the sediment that can be entrained by the streaming flow. Field observations and laboratory
26 experiments nevertheless indicate that the volume of sediment available for transport affects
27 their morphology. Here we present a theoretical model of the formation of small amplitude sand
28 dunes in steady currents accounting for the effects that the lack of sediment has on their formative
29 mechanisms and compare it against laboratory experiments and an application of a numerical
30 commercial model, thus enabling an improved understanding of the genesis of fluvial dunes in
31 sediment starved environments. Both models predict similar characteristics of starved dunes,
32 describing their lengthening with increasing irregularity in their spacing as their growth pro-
33 gressively exposes a motionless substratum. These findings agree with the results of laboratory
34 experiments and existing measurements of starved fluvial dunes in the field.

1 Introduction

River beds are seldom flat and those that contain sand generally exhibit a fascinating variety of bedforms, ranging from small-scale transverse ripples to large-scale longitudinal bars (Allen, 1968). Whenever the shear induced by water flowing over granular surfaces exceeds its threshold value for sediment motion, sediment particles begin to move and then sediment patterns might appear as a result of instability of the erodible river bed (Seminara, 2010). The flow of water and sediment produce these bedforms, which, in turn, profoundly influence water levels and sediment transport locally affecting mass and momentum transfer. In particular, transverse bedforms typically grow perpendicular to the main direction of the river stream and thus their presence is a primary source of flow roughness and a major factor in determining water levels (Engelund and Fredsoe, 1982). For practical purposes, the effect that these bedforms have on the hydrodynamics can be modelled as a hydraulic roughness of appropriate size. As such, unravelling the processes underlying their morphology is a subject of great concern to river engineering.

Fluvial dunes are one dimensional bedforms periodic in the longitudinal direction. They exhibit asymmetric profiles with fairly regular crests migrating invariably down-stream (Guy et al., 1966). Their typical crest-to-crest distances scale with the local water depth and their appearance is associated with subcritical flows in the Froude sense (Colombini, 2004). Because of their significance in formulating depth-discharge relations for river flows and predictor formulae for sediment transport, fluvial dunes received extensive attention from engineers and geomorphologists.

Many field observations and laboratory measurements indicate that sediment patterns commonly observed where large amounts of mobile sediment are available, i.e., alluvial bedforms, differ from those formed where mobile sediment is scarce, i.e., starved bedforms. Hereinafter we will refer to the latter conditions as sediment starvation. In fluvial environments sediment starvation is common. As channel slopes decrease, rivers typically exhibit abrupt transitions from gravel to sandy bottoms. In these transitional settings, seasonal and perennial streams subject to periods of low flow or discharge waves undergo a transient degradation until they are fully armoured (Parker et al., 1982). Then the natural formation of such armoured layer inhibits the entrainment of finer sediment from the bed, eventually resulting in sediment starvation. Whereby the armoured bed is developed and finer material continues to be supplied to the water flow, starved dunes may appear.

Recent advances in the physical modelling of fluvial starved bedforms revealed the effects of sediment starvation on bedform development. By means of a very simple phenomenological experiment, Venditti et al. (2017) described a definable sequence of starved bedforms emerging in steady currents depending on the supply of sediment. As the sediment supply from upstream increases, a gradual transition occurs starting from longitudinal sand ribbons to three-dimensional barchans that eventually coalesce onto amorphous sandy mounds ultimately leading to the generation of two-dimensional transverse dunes (Kleinhaus et al., 2002). However, still unclear is

73 how the lack of sediment affects the morphology of the resultant starved dunes. Only a few
74 observations are available (Carling et al., 2000a; Kleinhans et al., 2002; Venditti et al., 2019) and
75 measurements do not indicate a clear evolution in time. Same difficulty arises when modelling
76 the problem in the flume. The laboratory experiments of Tuijnder et al. (2009) show dune di-
77 mensions that progressively decrease as the volume of the finer mobile sediment decreases and
78 the immobile coarser underlayer is exposed. In contrast, the experimental data of Porcile et al.
79 (2020) describe starved dunes attaining longer wavelengths than their alluvial counterparts for
80 the same values of the hydrodynamic and morphodynamic parameters.

81 A first theoretical, process-based approach to the study of sand dune formation was proposed
82 by Kennedy (1969), who introduced the idea that fluvial dunes can be the result of a free
83 instability of a uniform steady flow over an alluvial bed. In the following decades, several
84 researchers investigated the formation of dunes and ripples by means of a linear stability analysis
85 (Engelund, 1970; Reynolds, 1976; Richards, 1980; Colombini, 2004; Colombini and Stocchino,
86 2011). An extensive review of the linear stability analyses of alluvial bed forms can be found in
87 Colombini and Stocchino (2012).

88 All these theoretical investigations consider an infinite availability of mobile sediment and
89 thus they are invalid in the case of sediment starvation. Blondeaux et al. (2016) and Porcile et al.
90 (2017) investigated the effects of sediment starvation on the formation of sea-wave ripples and
91 tidal dunes, respectively. They simulated the formation of small-amplitude starved bedforms in
92 oscillatory currents by means of an idealised model based on a stability analysis. Here a similar
93 theory is developed for steady currents, which can be considered as an extension of the linear
94 stability analysis of Colombini (2004) including the effect of sediment starvation. Our main
95 hypothesis is that when a motionless substratum is exposed by the formation of dunes, the lack
96 of sand affects the sediment transport, and, in turn, the dune morphology. By following the
97 modelling procedure outlined in Blondeaux et al. (2016), this hypothesis is formulated through
98 numerical means.

99 We apply this model to the formation of laboratory-scale sand dunes by assuming hydrody-
100 namic and sediment transport parameters in line with flume experiments previously performed at
101 the University of Genoa (Porcile et al., 2020). Model results describe the lengthening of starved
102 dunes with an increasing irregularity in their spacing as their growth progressively exposes the
103 unerodible substratum.

104 Secondly, we dropped the limiting assumption of small dune amplitudes with respect to the
105 local water depth, which is implicit in the linearization process, by performing a fully numerical
106 modelling of finite-amplitude starved dunes. We developed an application of the commercial
107 model Delft3D capable of describing the formation of sand dunes in steady currents while ac-
108 counting for sediment starvation. Analogously to the small-amplitude dune model, the presence
109 of a motionless substratum is included that can lead to sediment starvation depending on ini-
110 tial sediment availability and forcing conditions. Numerical results confirm the findings of the
111 linearized solution, thus suggesting that the lack of sediment available for transport dictates the

112 dimensions of fluvial dunes, potentially affecting the frictional force they exert on the overlying
113 flow.

114 This paper is organised as follows. Section 2 is devoted to a brief description of the ex-
115 perimental measurements of Porcile et al. (2020) that we used to provide controlled empirical
116 foundations for the development of process-based idealised models of the genesis of sand-starved
117 dunes in steady currents. In section 3.1 we formulate a stability analysis of sandy beds forced by
118 steady currents considering a limited availability of mobile sediment. In section 3.2 we introduce
119 a fully numerical model of the formation of finite-amplitude starved dunes. Section 4 present the
120 results of our modelling exercises. Then, these results are thoroughly compared with previous
121 laboratory measurements and field observations in section 5. Conclusions are drawn in section
122 6.

123 2 Background: Flume experiments by Porcile et al. (2020)

124 Porcile et al. (2020) described experimental measurements of the formation of starved dunes car-
125 ried out in a laboratory flume at the University of Genoa. These flume experiments were designed
126 to provide further data on the effects of sediment starvation on the formation of fluvial dunes and
127 to compare results of the present numerical investigation with laboratory measurements. Three
128 sets of experiments were performed by fixing all the hydrodynamic and morphodynamic param-
129 eters, except the thickness of the layer of sediment initially available for transport. The duration
130 of the experiments was also kept constant. Well-sorted sand characterised by a mean grain size
131 $d_s^* = 1.12 \text{ mm}$ was glued on the bottom of the flume, thus creating a rough bed. Before water
132 was pumped through the flume, the same sand was spread on the rough fixed bottom, generating
133 a sand layer with an initial uniform thickness Δ^* , that can be varied per experiment. This setup
134 allowed us to investigate the effects of sediment starvation alone by progressively decreasing the
135 thickness of the initial sand layer (see Porcile et al. (2020) for additional details on the apparatus
136 and experimental procedure).

137 The bed elevation recorded at the end of the experiments along the centerline of the flume
138 shows that well-defined sand dunes emerged from a uniform sand layer independently on the
139 initial sediment availability (Figure 1). When the emerging bedforms were not high enough to
140 expose the unerodable bottom of the flume, bed profiles of alluvial dunes were observed (Figure
141 1-top). Average wavelengths of these alluvial dunes were approximately the same during all the
142 experiments, showing triangular shapes with gentle stoss sides and steep lee sides. As soon as
143 the growth of the dunes led to the exposure of the flume bottom, regularly spaced transverse
144 dunes were replaced by bump-shaped starved bedforms with steep stoss and lee sides separated
145 by flat troughs (Figure 1-middle and 1-bottom).

146 Crest-to-crest distances of starved dunes markedly increased when starting off with a thinner
147 initial sand layer. An increasing irregularity associated to a decreasing thickness of the initial
148 sand layer was also observed. In some cases, the strongest sediment starvation resulted in the

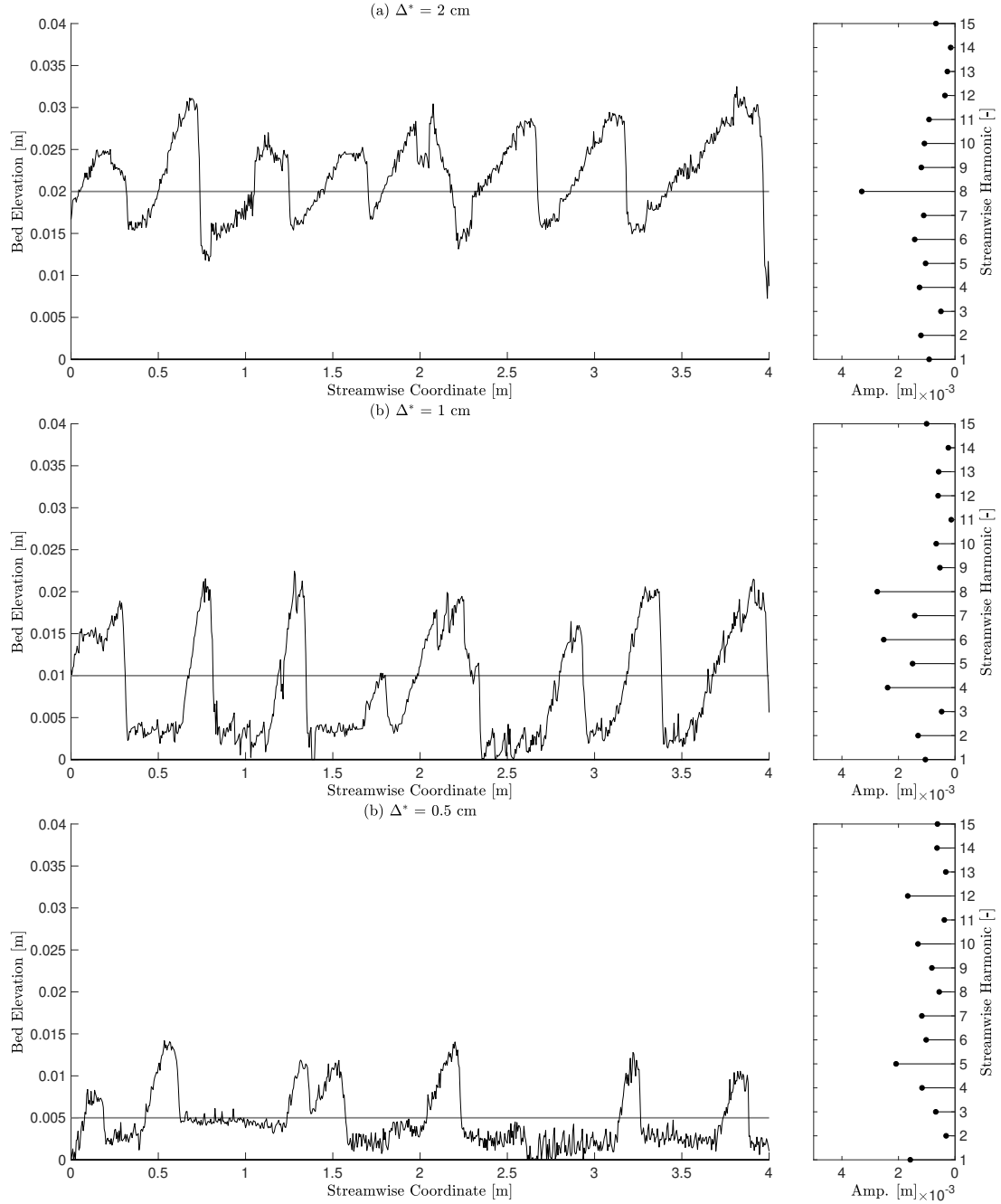


Figure 1: Laboratory measurements of Porcile et al. (2020). Left panels: final bottom configurations measured along the centerline of the flume for decreasing values of the initial uniform thicknesses of the sand layer $\Delta^* = 2$ cm (top), $\Delta^* = 1$ cm (middle) and $\Delta^* = 0.5$ cm (bottom). Forcing flow direction is from left to right. Thin black lines represent the bed elevations, thick black lines show the rigid bottom of the flume while thick grey lines show the initial level of the sand layer. Right panels: Spectra of the final bottom configurations. The amplitude of the Fourier components is plotted versus the streamwise harmonic.

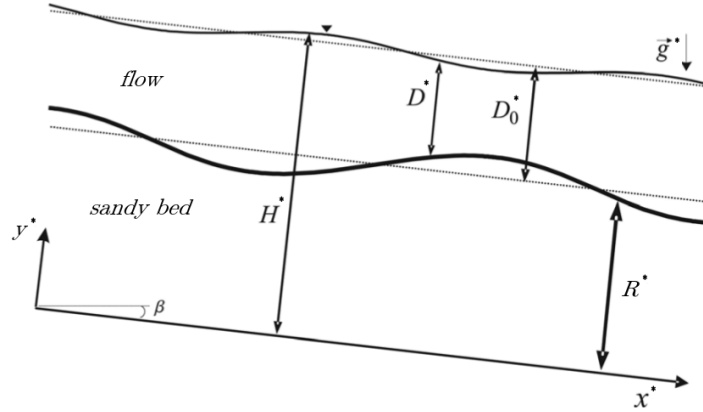


Figure 2: Sketch of the hydrodynamic modelling showing the sloping streamwise x^* -axis, the almost vertical y^* -axis pointing upwards, the local water depth D^* and the reference level R^* .

149 appearance of three-dimensional barchan dunes. The lengthening of starved bedforms is also
 150 shown by the Fourier spectra of the bottom profiles (Figure 1 right panels), which provide a
 151 measure of the increasing spacing of starved dunes and allow for a rough estimation of their
 152 average wavelength. Streamwise profiles of alluvial dunes were characterised by peak harmonic
 153 components corresponding to approximately 0.5 m average wavelength. The spectra of starved
 154 dunes show that the peak harmonic component shifts towards lower frequencies as the initial
 155 availability of sediment decreases, confirming their marked lengthening.

156 3 Methods

157 Here we describe both the quasi-linear model (subsection 3.1), whereby a linear flow model
 158 provides the stress field, a predictor relationship computes the associated sediment transport
 159 and the Exner equation is integrated numerically including the effect due to sediment starvation,
 160 and the fully nonlinear Delft3D model (subsection 3.2).

161 For both models, the flow of an incompressible fluid in a wide straight channel is considered
 162 and the Reynolds averaged Navier Stokes (RANS) equations on a vertical plane (2DV) together
 163 with the 1D form of the Exner equation are used to describe the hydrodynamics and the bed
 164 evolution, respectively.

165 3.1 Quasi-linear model

166 By adopting the so-called quasi-steady approximation, whereby the flow is assumed to adapt
 167 instantaneously to variations of the bed elevation, the solution of the morphodynamic problem
 168 can be split in two parts: i) the solution of the steady flow equations above a fixed periodic bed,
 169 which provides the flow response to a given bed perturbation in terms of the stress acting on the
 170 bed; ii) the solution of the Exner equation, which provides the evolution of the bed perturbation

171 in terms of propagation and amplification. An algebraic empirical relationship provides the link
 172 between these two steps, relating the local value of the net sediment transport to the local value
 173 of the stress acting on the bed.

174 In the quasi-linear model, at any given time, the spatially periodic bed topography is de-
 175 composed in a finite number of harmonics. Moreover, the amplitudes of the bed harmonics are
 176 assumed to remain small enough for the linear approximation to hold, so that the flow field is
 177 expressed as the superposition of the (linear) flow response to each of the bed harmonics. The
 178 bed stress distribution provided by the hydrodynamic module is then fed to the morphodynamic
 179 module, where the stress field is converted in a sediment discharge distribution. If part of the
 180 motionless substratum is exposed, a suitable numerical procedure is then employed, which cor-
 181 rects the sediment transport rate to account for the local unavailability of erodible sediment.
 182 Finally, the new bed topography is evaluated by means of a numerical integration of the Exner
 183 equation.

184 3.1.1 Hydrodynamic module

185 The formulation of the hydrodynamic module follows closely the one adopted by Colombini
 186 (2004) and by Colombini & Stocchino (2005, 2008), which is briefly summarized in the following.
 187 The interested reader is referred to the above works for the details of the flow model.

188 A steady, turbulent free-surface flow is considered in the domain sketched in Figure 2, whereby
 189 the streamwise x^* -axis is sloping with slope $S \equiv \tan(\beta)$ and the almost vertical y^* -axis points
 190 upwards (hereinafter an asterisk denotes dimensional quantities). The free-surface is represented
 191 by the curve $y^* = R^* + D^*$, where D^* is the local water depth and R^* indicates the reference level,
 192 i.e., the average level at which conventionally the mean logarithmic velocity profile vanishes. This
 193 level represents the interface between the fluid flow and the river bed and depends primarily on
 194 the bottom roughness.

195 The triplet composed by the (constant) fluid density ρ^* and by the uniform flow depth D_0^*
 196 and shear velocity $u_{\tau 0}^*$ is used for nondimensionalization.

197 Neglecting the viscous stresses, the steady, dimensionless 2DV RANS and continuity equa-
 198 tions read

$$199 \quad U \frac{\partial U}{\partial x} + V \frac{\partial U}{\partial y} = -\frac{\partial P}{\partial x} + \frac{SC^2}{\text{Fr}^2} + \frac{\partial T_{xx}}{\partial x} + \frac{\partial T_{xy}}{\partial y}, \quad (1)$$

$$200 \quad U \frac{\partial V}{\partial x} + V \frac{\partial V}{\partial y} = -\frac{\partial P}{\partial y} - \frac{C^2}{\text{Fr}^2} + \frac{\partial T_{xy}}{\partial x} + \frac{\partial T_{yy}}{\partial y}, \quad (2)$$

$$\frac{\partial U}{\partial x} + \frac{\partial V}{\partial y} = 0, \quad (3)$$

201 where P is the ensemble-averaged pressure and (U, V) are the ensemble-averaged velocity com-
 202 ponents in the x and y directions, respectively. Moreover, T_{ij} are the dimensionless Reynolds

203 stresses

$$\mathbf{T} = \begin{bmatrix} T_{xx} & T_{xy} \\ T_{yx} & T_{yy} \end{bmatrix} = \begin{bmatrix} 2\nu_T \frac{\partial U}{\partial x} & \nu_T \left(\frac{\partial U}{\partial y} + \frac{\partial V}{\partial x} \right) \\ \nu_T \left(\frac{\partial U}{\partial y} + \frac{\partial V}{\partial x} \right) & 2\nu_T \frac{\partial V}{\partial y} \end{bmatrix}, \quad (4)$$

204 and ν_T is the dimensionless turbulent eddy viscosity.

205 Two parameters are generated by the nondimensionalization procedure, namely the Froude
 206 number $\text{Fr} = U_0^*/\sqrt{g^*D_0^*}$ and the conductance coefficient $C = U_0^*/u_{\tau 0}$, where U_0^* is the area
 207 velocity of the base uniform flow and g^* is the gravitational acceleration. These two parameters
 208 are related to one another by the uniform-flow law, yielding:

$$u_{\tau 0}^* = \frac{U_0^*}{C} = \sqrt{g^*D_0^*S} \quad \Rightarrow \quad C = \frac{U_0^*}{u_{\tau 0}^*} \simeq \frac{\text{Fr}}{\sqrt{S}}. \quad (5)$$

209 Furthermore, the coordinate transformation

$$\xi = x, \quad \eta = \frac{y - R(x)}{D(x)}, \quad (6)$$

210 is introduced, which maps the flow domain of Figure 2 into a rectangular domain.

211 The turbulent eddy viscosity ν_T is expressed in terms of an algebraic mixing length L as

$$\nu_T = \frac{1}{D} \frac{\partial U}{\partial \eta} L(\eta)^2, \quad L(\eta) = \kappa D(\eta + \eta_R)(1 - \eta)^{1/2}, \quad \eta_R = \frac{2.5d_s}{30}, \quad (7)$$

212 where η_R is the roughness height, which is assumed to be proportional to the non dimensional
 213 roughness and, ultimately, to the dimensionless sediment diameter d_s .

214 The problem is then closed by an appropriate set of boundary conditions. In particular, at
 215 the reference level the velocity components vanish according to the no-slip condition

$$U = 0, \quad V = 0 \quad \text{at} \quad \eta = 0, \quad (8)$$

216 whereas at the free surface, the kinematic boundary condition reads

$$-U \left(\frac{\partial R}{\partial x} + \frac{\partial D}{\partial x} \right) + V = 0 \quad \text{at} \quad \eta = 1. \quad (9)$$

217 and the dynamic boundary condition yields

$$T_N = 0, \quad T_T = 0 \quad \text{at} \quad \eta = 1, \quad (10)$$

218 where T_N and T_T represent the normal and tangential components of the stress acting on a
 219 surface at constant η , respectively. Finally, periodic boundary conditions are enforced at the
 220 upstream and downstream sides of the domain.

221 3.1.2 Perturbation method

222 Assuming that the height of the dunes is much smaller than the local water depth, the flow field
 223 can be evaluated by means of a perturbation approach. As far as the formation of regularly
 224 spaced dunes is concerned, it is also possible to assume the periodicity of the bottom geometry.
 225 The sandy bed can then be expressed as superposition of different spatial components. Of note,
 226 with the goal of extending the analysis to starved dunes, the number of spatial components
 227 should be large enough to properly describe those transition regions where the exposition of
 228 the unerodible substratum occurs. Presently, the following normal-mode representation for the
 229 perturbed variables is adopted

$$F(\xi, \eta) = F_0(\eta) + \epsilon F_1(\xi, \eta) = F_0(\eta) + \epsilon f(\eta)e^{i\alpha\xi} + c.c., \quad (11)$$

230 where ϵ is a small parameter and α denotes the longitudinal dimensionless wavenumber of the
 231 perturbation.

232 Substituting the above splitting into the system of equations (1)-(3) and boundary conditions
 233 (8)-(10) and collecting terms at the same order of magnitude in ϵ , a set of ordinary differential
 234 equations is derived at $\mathcal{O}(\epsilon)$. The resulting two-points boundary value problem is eventually
 235 solved by means of a shooting method. In particular, the flow response to a perturbation of the
 236 bed of amplitude r can be determined in terms of the shear stress t_{tb} evaluated at the saltation
 237 level η_B , which represents the interface between the flowing fluid and the saltation layer, i.e., the
 238 thin bottom layer where bedload transport takes place (Colombini, 2004). Moreover, the saltation
 239 level is assumed parallel to the reference level at a distance equal to the bedload layer thickness

$$\eta_B - \eta_R = l_B d_s = \left\{ 1 + a_B \left(\frac{T_{TR} - T_{TC}}{T_{TC}} \right)^{m_B} \right\} d_s. \quad (12)$$

240 where T_{TR} and T_{TC} are the shear stress evaluated at the reference level and its critical threshold
 241 for incipient motion. The empirical parameters a_B , m_B have been set equal to 1.42 and 0.64,
 242 respectively (Colombini and Stocchino, 2008).

243 As expected from a linear, normal-mode analysis, we eventually obtain:

$$t_{tb} = t_t(\eta_B) = r \widehat{t}_{tb} \quad (13)$$

244 where \widehat{t}_{tb} only depends on the wavenumber α and on the flow parameters Fr and C (see Colombini
 245 (2004) for the details of the above procedure).

246 3.1.3 Morphodynamic module

247 In the present formulation, suspended sediment transport is neglected and only bed-load trans-
 248 port is considered, i.e., sliding, rolling and saltating grain particles. Such an assumption seems
 249 reasonable since sand dunes are more likely to appear in sub-critical flows (Fredsoe, 1974), the

250 bottom shear stress generated by which do not usually produce large suspension of sediment. A
 251 common and useful approach to the quantification of bedload transport is to empirically relate
 252 the volumetric sediment transport rate per unit width q_S^* with the difference between the bottom
 253 shear stress T_{TB}^* and the critical threshold value for incipient motion T_{TC}^* . A large number of
 254 empirical relations have been derived using flume data from many laboratory experiments, and
 255 these share the structure

$$\frac{q_S^*}{\sqrt{(s-1)g^*d_s^{*3}}} = \Phi(\Theta_B, \Theta_C), \quad (14)$$

256 where $s = \rho_s^*/\rho^*$ is the relative density of the sediment, Φ is the dimensionless bed-load transport
 257 rate and Θ_B is the Shields parameter built upon the bed shear stress at level B . More precisely,
 258 we have:

$$\Theta_B = \frac{T_{TB}^*}{g^*\rho^*(s-1)d_s^*} = T_{TB}\Theta_{R0}, \quad \Theta_{R0} = \frac{S}{(s-1)d_s}, \quad (15)$$

259 where Θ_{R0} is the Shields parameter evaluated at the reference level for the base uniform flow.

260 Among the commonly adopted bed-load transport predictors is the Fernandez Luque and
 261 Van Beek (1976) formula, which reads

$$\Phi = 5.7(\Theta_B - \Theta_C)^{3/2} \quad \text{if } \Theta_B > \Theta_C, \quad \Phi = 0 \quad \text{if } \Theta_B \simeq \Theta_C. \quad (16)$$

262 This predictor relation is presently employed as it appears to contain the main physical ingredi-
 263 ents controlling the process of sediment transport for values of the Shields parameter close to its
 264 threshold. Furthermore, the bed material tested in the experiments, on which the above relation
 265 is based, included different grain sizes ranging from sand to gravel.

266 Since the problem under consideration accounts for the presence of bottom perturbations, the
 267 bed is not flat and the stabilising effect of gravity, which opposes uphill motion and favours down-
 268 hill motion, is considered by correcting the threshold Shields stress Θ_C (Fredsoe and Deigaard,
 269 1992)

$$\Theta_C = \Theta_{CH} \left[1 - \left(S - \frac{\partial B}{\partial \xi} \right) \frac{1}{\mu_d} \right], \quad \text{with } \Theta_{CH} = 0.038, \quad (17)$$

270 where Θ_{CH} is the value for vanishing slope and μ_d is a dynamic friction coefficient, which has been
 271 set equal to one half of the Coulomb coefficient μ_c following the recommendations by Fredsoe and
 272 Deigaard (1992). Moreover, $\mu_c = \tan(\Psi)$ and Ψ represents the angle of repose of the sediment.
 273 For natural sediments, the angle of repose Ψ ranges between 30° and 50° resulting in friction
 274 coefficient μ_c ranging between 0.58 and 1.2. In this study we have employed $\mu_c = 1.0$.

275 Finally, the development of small-amplitude bottom perturbations can be estimated by the
 276 sediment continuity equation, which states that the positive (negative) divergence of the sediment
 277 transport rate is locally balanced by the decrease (increase) of the bottom elevation

$$\frac{\partial R}{\partial T} = -\frac{\partial \Phi}{\partial \xi}, \quad T = \frac{t^* \sqrt{(s-1)g^*d_s^{*3}}}{D_0^{*2}(1-p)}, \quad (18)$$

278 where T is a slow morphodynamic time coordinate.

279 3.1.4 Linearization

280 Under the hypothesis of small amplitude bed perturbations, the algebraic relationships (15-17)
281 can be linearized, providing the linear response of the flow to a given bed perturbation in terms
282 of the equilibrium (at capacity) sediment discharge.

283 In particular, we expand the bedload discharge Φ , the Shields parameter Θ_B and its critical
284 value Θ_C as in (11)

$$\Phi(\xi) = \Phi_0 + \epsilon\phi e^{i\alpha\xi} + c.c. , \quad (19)$$

$$\Theta_B(\xi) = \Theta_{B0} + \epsilon\theta_b e^{i\alpha\xi} + c.c. = \Theta_{R0} \left[1 - \eta_B + \epsilon t_{tb} e^{i\alpha\xi} + c.c. \right] , \quad (20)$$

$$\Theta_C(\xi) = \Theta_{C0} + \epsilon\theta_c e^{i\alpha\xi} + c.c. = \Theta_{CH} \left[1 - \frac{S}{\mu_d} + \epsilon i\alpha \frac{1}{\mu_d} r e^{i\alpha\xi} + c.c. \right] . \quad (21)$$

287 At the leading order in ϵ , we eventually obtain

$$\phi = \left(\frac{\partial\Phi}{\partial\Theta_B} \right)_0 (\theta_b - \theta_c) = \left(\frac{\partial\Phi}{\partial\Theta_B} \right)_0 \left(\Theta_{R0} \hat{t}_{tb} - \Theta_{CH} \frac{i\alpha}{\mu_d} \right) r = \hat{\phi} r \quad (22)$$

288 where, as for (13), the complex quantity $\hat{\phi}$ only depends on the wavenumber α and on the flow
289 and the sediment parameters for the base state.

290 Let us now consider the case of infinite availability of sediment, which corresponds to a
291 motionless unerodible substratum low enough for not being exposed by the erosive action of the
292 flow. In this case, with the additional hypothesis of small amplitude of the bed perturbation, the
293 Exner continuity equation (18) can be linearized and the classic normal mode stability analysis
294 is recovered. To this end, the reference level R is expanded as

$$R(\xi, T) = R_0 + \epsilon R_1(\xi, T) = R_0 + \epsilon r(T) e^{i\alpha\xi} + c.c. \quad (23)$$

295 and substituted in (18) to obtain the dispersion relationship

$$\frac{1}{r} \frac{dr}{dT} = -i\alpha \frac{\phi}{r} = -i\alpha \hat{\phi} \Rightarrow r(T) = e^{-i\alpha \hat{\phi} T} = e^{\Omega T} e^{-i\alpha \omega T} , \quad (24)$$

296 where $\hat{\phi}$ represents the complex wavespeed of the perturbation and

$$\omega = \text{Re} \left(\hat{\phi} \right) , \quad \Omega = \alpha \text{Im} \left(\hat{\phi} \right) , \quad (25)$$

297 are the celerity and growth rate of the bed perturbation, respectively.

298 An exponential dependence of the solution on time emerges, as expected in a linear stability

299 analysis. The growth rate is found to be

$$\Omega = \alpha^2 \Theta_{R0} \left(\frac{\partial \Phi}{\partial \Theta_B} \right)_0 \left(\frac{\text{Im}(\hat{t}_{tb})}{\alpha} - \frac{\Theta_{CH}}{\Theta_{R0} \mu_d} \right), \quad (26)$$

300 which clearly shows how the emergence of small-amplitude dunes is related to a balance between
 301 the destabilising effect due to the steady current, represented by the shear stress at the bed-load
 302 level, and the stabilising effect due to the gravity, represented by the dynamic friction coefficient.
 303 Thus the study of the dispersion relationship allows growing modes with positive growth rate
 304 to be identified in the parameter space and, among those, the fastest growing one. Finally, an
 305 estimate of the wavelength of the emerging dunes can be predicted by assuming that this most
 306 unstable mode prevails on the others during the short-term morphodynamic evolution of the
 307 sandy bed.

308 3.1.5 Modification to account for sediment starvation

309 When a motionless substratum is exposed by the formation of sand dunes, the lack of sediment
 310 affects its transport, and, in turn, the pattern morphology. The exposure of the motionless
 311 substratum locally prevents the entrainment of sediment, leading to sediment starvation. The
 312 sediment transport formula (16) quantifying the bed-load sediment transport cannot be applied
 313 in the case of sediment starvation unless a suitable numerical procedure is introduced capable of
 314 account for the local lack of mobile sediment.

315 Where sand is available, the sediment transport depends only on the bed shear stress. If the
 316 shear decreases (increases) in the flow direction, the sediment transport rate can be predicted
 317 by the predictor formula and some deposition (erosion) occurs according to the continuity of the
 318 sediment phase. Differently, where a motionless substratum is locally exposed, the amount of
 319 sediment in motion might be smaller than the local transport capacity. In particular, the value
 320 of the sediment transport rate $\Phi(x^*)$ depends not only on the value of the shear stress $\Theta_B(x^*)$
 321 but also on its spatial derivative. On the one hand, if the shear stress increases in the direction of
 322 the flow, the sediment transport rate remains constant since the flow cannot entrain additional
 323 mobile sediment since it is not available. On the other hand, if the shear stress decreases in
 324 the direction of the flow, two different scenarios are possible depending on the upstream value
 325 of the sediment transport rate. If the upstream value of the sediment transport rate is smaller
 326 than the local value predicted by the predictor formula $\Phi_P(x^*)$ the local sediment transport rate
 327 should be assumed equal to its upstream value. This can occur due to the upstream exposure
 328 of the motionless substratum. Otherwise, the sediment transport rate can be predicted by the
 329 predictor formula and some deposition of sediment over the exposed substratum should occur.

$$\left. \frac{d\Phi}{dx^*} \right|_+ = 0 \quad \text{if} \quad \left. \frac{d\Theta_B}{dx^*} \right|_{x^*} > 0, \quad (27)$$

330

$$\left. \frac{d\Phi}{dx^*} \right|_+ = 0 \quad \text{if} \quad \left. \frac{\Theta_B}{dx^*} \right|_{x^*} < 0 \quad \text{and} \quad \Phi(x^*) < \Phi_P(x^*), \quad (28)$$

331

$$\Phi(x^*) = \Phi_P(x^*) \quad \text{if} \quad \left. \frac{\Theta_B}{dx^*} \right|_{x^*} < 0 \quad \text{and} \quad \Phi(x^*) > \Phi_P(x^*). \quad (29)$$

332

333

334

335

336

337

338

339

340

341

342

343

344

345

346

347

348

349

350

351

352

These simple rules (27)-(29) introduce strong nonlinearities and the time development of the bottom configuration can be obtained only by numerical means. The present model integrates in time and space the dimensionless sediment continuity equation. The time advancement of (18) is solved by means of a Runge-Kutta second order approach, while the spatial derivatives are replaced by their second order finite difference approximations. A computational domain of length L_d^* along the horizontal axis x^* is considered and periodic boundary conditions are applied at its ends. The dimensionless length of the computational domain $L_d = L_d^*/D_0^*$ and the thickness of the initial sand layer $\Delta = \Delta^*/D_0^*$ are free geometrical parameters. The value of L_d should be large enough to assume its influence on the time development of the bottom configuration to be negligible and to properly represent the formation of the fastest growing mode predicted by the linear stability analysis. Since the time development of the entire range of unstable modes has to be described with sufficient accuracy, the spatial discretization should be accurate enough to represent the smaller wavelength of the unstable modes predicted by the linear stability analysis with a suitable number of computational points.

In those transition regions between the motionless substratum and the erodible bed, small-scale spurious oscillations arise as a result of the Gibbs' effect associated with the discontinuity in the bed slope. In its numerical time-stepping, the model forces the bed elevation to never drop below the substratum's level by applying a filtering procedure removing the small-scale spurious oscillations. The results of preliminary simulations repeated halving grid size, time step and domain length indicate that the chosen couple of values does not affect the time development of the bottom configuration.

353

3.2 Fully nonlinear model

354

3.2.1 General model description

355

356

357

358

359

360

361

362

363

The finite-amplitude evolution of fluvial dunes in sediment scarce environments is modelled in the numerical shallow water model Delft3D (Lesser et al., 2004). Analogous to the small-amplitude model, the hydrodynamic equations (here in terms of vertical σ -coordinates) consist of the 2DV Navier Stokes equations, a continuity equation and a turbulence closure model, supplemented by appropriate boundary conditions. In contrast to the small-amplitude model, turbulence is modelled by means of the $k_T - \epsilon_T$ turbulence model, in which both the turbulent kinetic energy per unit volume k_T and the dissipation rate per unit volume ϵ_T are computed. Both the bed load and the suspended load are included in the model, and bed evolution is computed by the Exner equation. For an overview of the relevant 2DV model equations, see e.g. Damveld et al.

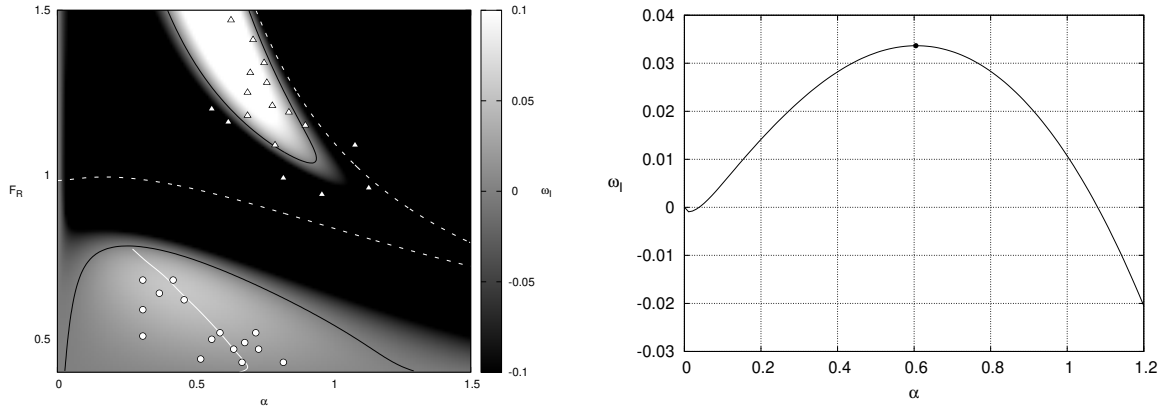


Figure 3: Results of the quasi-linear model in the case of an unlimited sediment supply. Left panel: growth rate plotted in shades of grey for a value of the conductance coefficient $\mathcal{C} = 15$. Thick black lines represent the curves of vanishing growth rate, dashed white lines represent the curves of vanishing celerity, white line represent fastest growing modes. The marks indicate the experimental measurements of Guy et al. (1966): circles, dunes; triangles, antidunes. Right panel: growth curve for a value of the Froude number $Fr = 0.5$ whose maximum identifies the fastest growing mode.

364 (2020).

365 3.2.2 Model domain, boundary conditions and parameter choices

366 The horizontal length of the domain is 60 m long and has a uniform grid spacing of 2.5 cm. In
 367 the vertical direction the grid consists of 30 σ -layers, with a small thickness (0.25% of the local
 368 water depth D^*) near the bed, gradually increasing in the upward direction. At the upstream
 369 lateral boundary a logarithmic velocity profile with a constant discharge of $0.03 \text{ m}^3/\text{s}$ is specified,
 370 whereas at the downstream lateral boundary the water level is kept constant throughout the
 371 simulations at a level of 12 cm. These values lead to a Froude number $Fr = 0.51$, similar to those
 372 characterising the flume experiments. The vanishing of the stress tensor was imposed at the free
 373 surface. The area of interest is situated in the second half of the domain to ensure that possible
 374 upstream boundary disturbances do not migrate into the domain and influence the results. The
 375 hydrodynamic time step is set equal to 0.15 seconds and a spin-up time of 10 minutes is made
 376 during which no bed level changes are allowed. Finally, the roughness of the bed is specified
 377 through a roughness length z_0 of 1 mm, which is equal to the sediment diameter. Note that the
 378 bed roughness does not change when the bare substrate is exposed, which is in fact in line with
 379 the experimental setup, where sediment was glued to the bottom of the flume (Porcile et al.,
 380 2020).

381 4 Results

382 Generally, comparing theoretical results of stability analyses with laboratory measurements is
383 difficult. Since the flume width is usually of the same order of the flow depth, the side walls
384 affect the bottom shear stress. If the bottom is rougher than the side walls, as in the experiments
385 by Porcile et al. (2020), the distribution of the shear along the wetted perimeter of the channel
386 is nonuniform. As such, experimental outcome cannot be expected to correspond to theoretical
387 findings based on the assumption of a wide open-channel flow, unless a correction for the shear
388 stress at the side walls is made. An equivalent, uniform open-channel flow characterising the flume
389 experiments can be evaluated by the side-wall correction (Vanoni and Brooks, 1957). Partitioning
390 the flume cross-section into a hydraulically rough and a smooth sub-regions corresponding to the
391 bottom and the side walls, respectively, and solving iteratively a system of implicit equations
392 including the water continuity, the Keulegan equations for smooth and rough flow regimes and
393 the Rouse equation, the side-wall correction determines a uniform, wide open-channel flow, which
394 is related to the uniform flow realised in the narrow flume. Then, it is possible to evaluate its
395 principal unknowns of interest. Particularly useful for a comparison with the linear stability
396 analysis is the equivalent Froude number and the representative conductance coefficient. It is
397 worth nothing that the Froude numbers characterising the equivalent open-channel flows related
398 to the individual experiments turn out to be larger than their measured values. This experimental
399 post-process is crucial to generalise the results of lab-scale flows by defining global dimensionless
400 quantities of interest which are independent of the flume width. As such, the side-wall correction
401 allows for comparing the experimental results with the modelling of small-amplitude dunes.

402 4.1 Quasi-linear model results

403 The investigation of the dispersion relationship (23) allows possible instability regions to be
404 isolated in the parameter space. Among the free parameters of the stability-based model, there
405 are the unperturbed flow depth D_0^* and the uniform mean grain size of the sediment d_s^* , which
406 determine the conductance coefficient characterising the unperturbed steady stream. In order
407 to compare the laboratory observations with the average wavelength of small-amplitude alluvial
408 dunes predicted by the stability analysis, the value of the mean grain size was set equal to that
409 of the well-sorted sediment used in the experiments. The unperturbed mean water depth was set
410 equal to the uniform depth of the wide open channel flow evaluated by the side-wall correction.
411 Then, the values of the conductance coefficient and the Froude number can be easily evaluated
412 ($C = 15, Fr = 0.5$) for the unperturbed flow.

413 Varying the Froude number, it is possible to compute the growth rate ω_I as well as the value
414 of ω_R which determines the perturbation celerity as function of the dimensionless wavenumber
415 α (see Figure 3). Positive values of the growth rate represent the growth of small-amplitude
416 perturbations, thus indicating instability. On the other hand, the value of ω_R determines the
417 perturbations' celerity, positive (negative) values indicating downstream (upstream) migration.

418 In left panel of Figure 3 the broken white lines represent vanishing values of the migration
419 rate. Below the lower broken line the celerity of the growing modes is positive (i.e. downstream
420 migration, alluvial dunes). The growing modes lying above this line has negative celerity (i.e.
421 upstream migration, alluvial antidunes). The good agreement between the identified regions
422 of instability and the experimental dataset of Guy et al. (1966) later ‘side-wall corrected’ by
423 Colombini (2004) prove the reliability of the stability analysis. Our experimental data fall within
424 the appropriate region of instability corresponding to some of the smaller (wavelengths) dunes
425 observed by Guy et al. (1966).

426 From the previous plot in the left panel of Figure 3, it is possible to extrapolate the growth
427 curve shown in the right panel of Figure 3 by considering the value of the Froude number of the
428 experiments. Hence, the fastest growing mode can be selected among the range of the predicted
429 perturbations. Assuming that this mode prevails over the short-term morphodynamic evolution
430 of the sandy bed, the wavelength of the small-amplitude dunes can be predicted. For the chosen
431 set of parameters the stability analysis predicts the appearance of bottom perturbations charac-
432 terised by a wavenumber $\alpha = 0.6$, which corresponds to a value of the dimensional wavelength
433 slightly smaller than $\lambda^* = 1 \text{ m}$. This value is of the same order of the wavelengths of the alluvial
434 dunes observed during the experiments, though an overestimation is present.

435 To test whether the model can provide a reliable description of the genesis of small-amplitude
436 starved dunes as observed during the flume experiments, a series of simulations is performed
437 computing the time development of an initial random bottom waviness forced by a uniform
438 steady current by fixing the hydrodynamic and morphodynamic parameters and varying only
439 the supply of sediment. Analogously to the experimental investigation, the sediment supply is
440 decreased by decreasing the thickness Δ of the initial sand layer through which dunes can develop.
441 Figure 4 shows the bottom configurations at the beginning (grey lines) and at the end (black
442 lines) of each numerical simulation. The values of the Froude number and the conductance
443 coefficient are kept constant during all the numerical simulations and equal to those of the
444 experiments evaluated by means of the side-wall correction. The dimensionless length L_d of the
445 computational domain is equal to 100 and the dimensionless thickness of the initial sand layer
446 is progressively decreased starting from $\Delta = 0.2$ down to $\Delta = 0.05$. Since the experiments are
447 characterized by a dimensional mean water depth $D_0^* = 0.1 \text{ m}$, the value of Δ^* ranges from 2
448 cm to 0.5 cm and the dimensional length of the computational domain is about 10 metres. Each
449 numerical simulation is made considering a dimensionless simulation time that is of the same
450 order of magnitude as that of the experiment duration. At the beginning of the first simulation
451 (Figure 4, panel A) the bottom is characterised by a random perturbation of small amplitude.
452 Then, the computed bottom profile shows a rapid decay of the perturbation components of very
453 small wavelengths and only the unstable modes predicted by the stability analysis survive. Then,
454 for long time, the growth of the fastest growing mode gives rise to periodic bedforms (dunes).
455 The growth of dunes is exponential and for $\Delta = 0.2$, the appearance of the bottom forms does
456 not bare the motionless substratum. At the end of the simulation, ten clearly defined dunes can

457 be easily identified through the computational domain with an average dimensional wavelength
458 equal to ten. Different results are obtained in the second and third simulations (see panels B
459 and C of 4). These results correspond to a dimensionless initial sand layer thickness equal to
460 0.1 and 0.05, respectively. Progressively decreasing the amount of the sediment available for
461 transport, the motionless substratum is exposed by the growth of the dunes, leading to sediment
462 starvation. Starved dunes show increasing crest-to-crest distances as the degree of sediment
463 starvation increases. Their general lengthening and the increasing irregularity of their profile is
464 evident.

465 The panels on the right-hand side of Figure 4 show one-dimensional spectra of the final
466 bottom profiles computed by the stability-based model. The modulus of the complex amplitude
467 of each harmonic component of the Fourier transform of the bottom elevation is presented.
468 These spectra reveal whether a dominant wavelength can be identified or whether the bottom
469 configuration is the result of a superposition of many different components. By comparing the
470 harmonic content of each computed bed profile, it is seen that the peak harmonic component
471 shifts towards lower frequencies as the thickness of the initial sand layer decreases.

472 4.2 Fully nonlinear model results

473 Next, we repeat our numerical experiments with the finite-amplitude model. Again, the only
474 parameter which is varied is the initial sediment thickness. Figure 5 (left-hand panels) show
475 the initial and final bottom configurations of the simulations. For the sediment abundant case
476 (panel a), asymmetrically-shaped dunes develop, with an average crest-to-crest distance slightly
477 larger than $\lambda^* = 1m$. Similar to the small-amplitude result, this value is of the same order as
478 that observed during the experiments. Panels (c) and (e) of Figure 5 show a decreasing number
479 of dunes as a result of the decreasing sediment availability. In contrast to the small-amplitude
480 result, the wave height and spacing of the patterns become more regular over time, especially
481 in the sediment scarce case. This is a good indication that the bottom configuration is close to
482 their equilibrium state. Another effect which can be observed towards the end of the simulations
483 is the decrease of asymmetry of the (isolated) bedforms, which are characterized by a shorter
484 stoss side.

485 Similar to the results of the small-amplitude simulations, the right-hand panels of Figure
486 5 show the moduli of the Fourier components. Also in this case, it can be observed that the
487 peak shifts towards the lower wavenumbers as the sediment thickness decreases. However, this
488 observation is less apparent than in the former case. Due to asymmetrical shape of the patterns,
489 the harmonic signal is composed of a much broader spectrum, such that no particular peak
490 stands out.

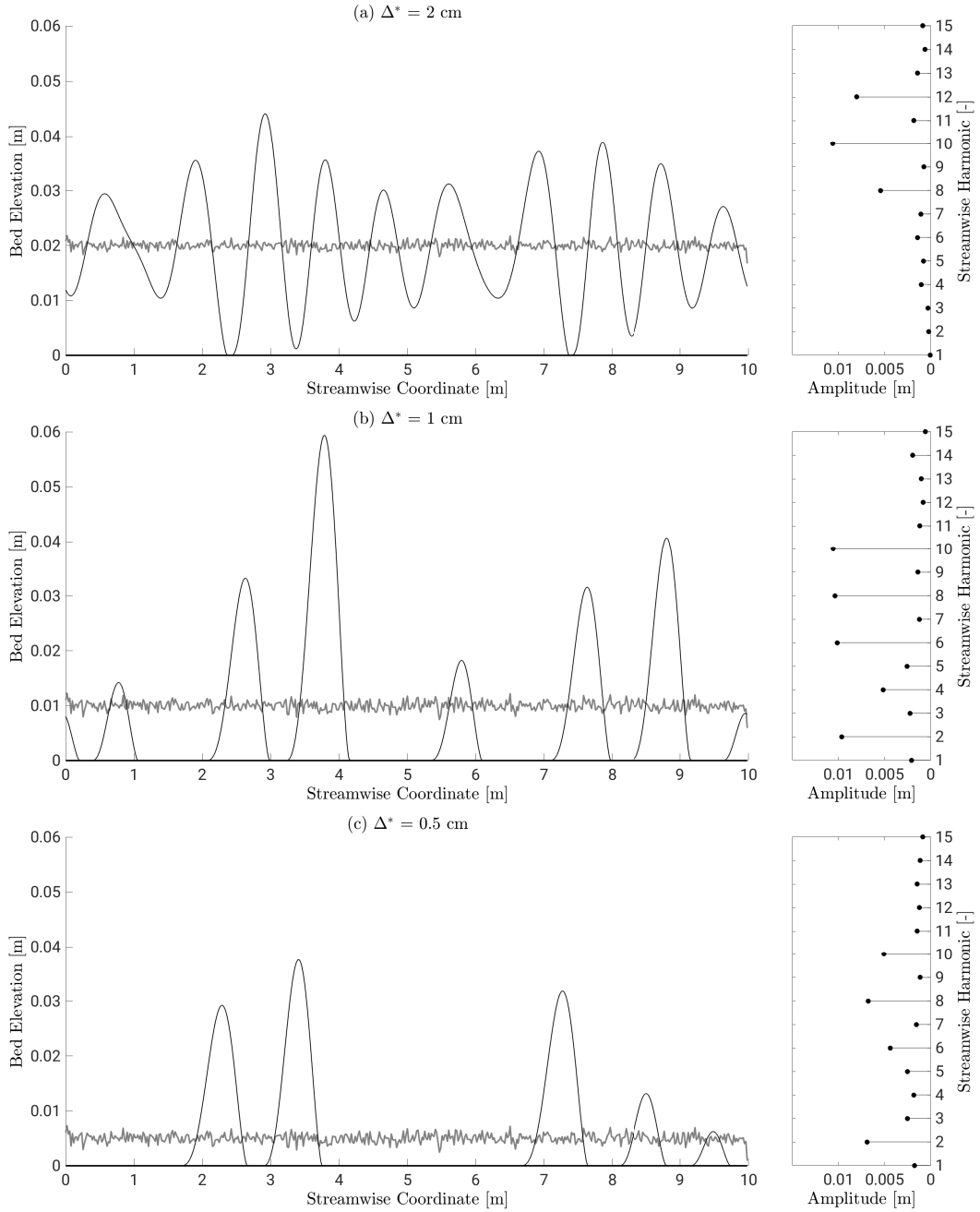


Figure 4: Results of the quasi-linear model in the case of a limited sediment supply. Left panels: Time development of an initial random bottom waviness for the values of dimensionless parameters $\mathcal{C} = 15$ and $\text{Fr} = 0.5$ and decreasing values of initial uniform thicknesses of the sand layer. Thin black lines represent the final bottom configurations computed by the model, thick black lines show the motionless bottom while thin grey lines show the initial random waviness. Right panels: Spectra of the final bottom configurations. The amplitude of the Fourier components is plotted versus the streamwise harmonic.

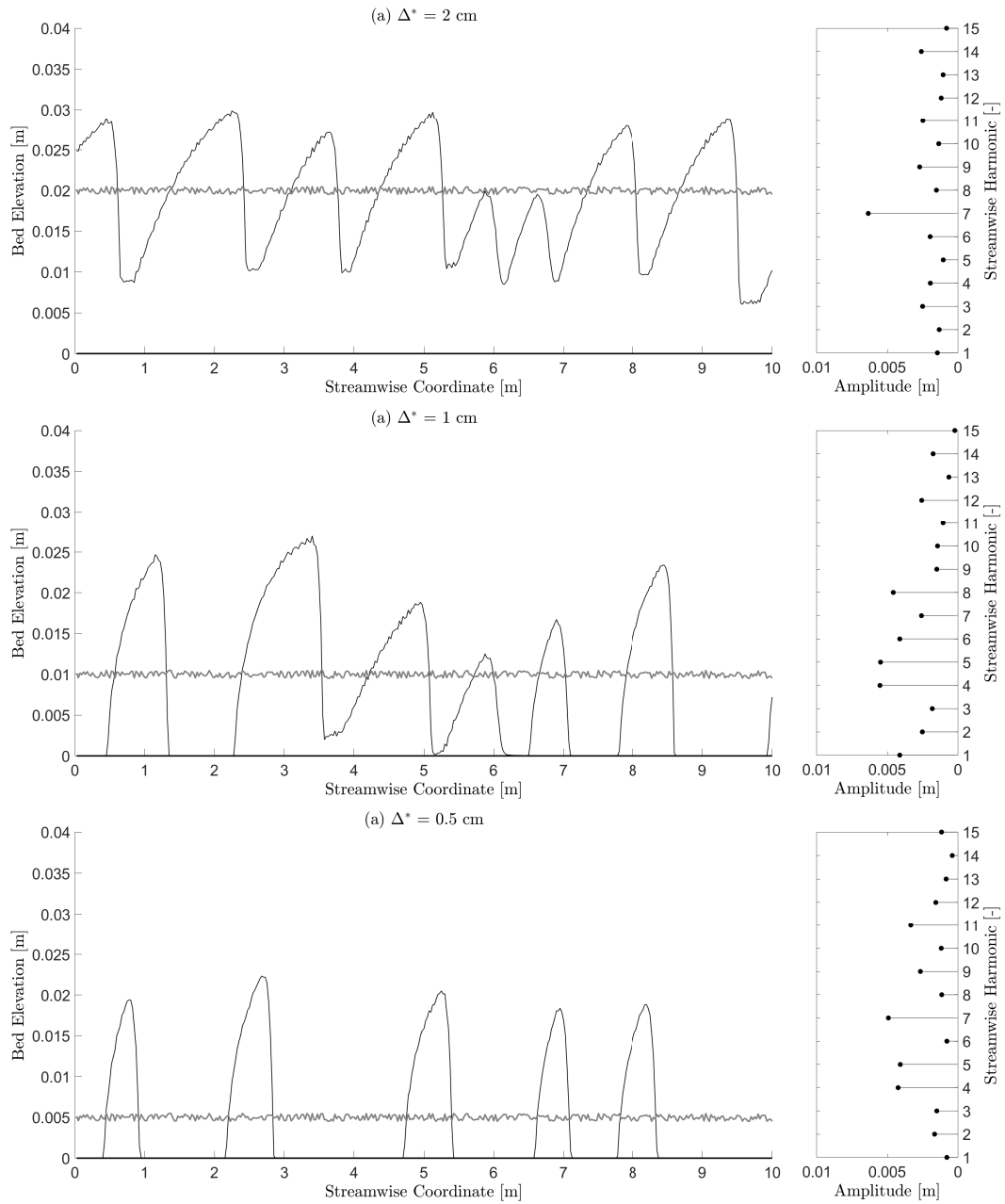


Figure 5: Results of the fully nonlinear Delft3d model in the case of a limited sediment supply. Left panels: Time development of an initial random bottom waviness decreasing values of initial uniform thicknesses of the sand layer. Thin black lines represent the final bottom configurations computed by the model, thick black lines show the motionless bottom while thin grey lines show the initial random waviness. Right panels: Spectra of the final bottom configurations. The amplitude of the Fourier components is plotted versus the streamwise harmonic.

491 **5 Discussion**

492 The idealised process-based models described in the previous sections provide support for the
 493 experimental findings of Porcile et al. (2020). Particularly, the models reproduce the same
 494 observed effects of sediment starvation on the genesis of sand dunes in steady currents when
 495 an unerodable bottom is exposed by the growth of the bedforms. Both a stability analysis
 496 based on the numerical simulation of small amplitude perturbations of the bottom configuration
 497 and a fully numerical commercial code able to simulate the time development of finite amplitude
 498 bedforms predict the lengthening of sediment starved dunes as their growth progressively exposes
 499 the motionless substratum, with increasing irregularity of their morphology and spacing. Despite
 500 the overestimation of alluvial dune wavelength obtained by using these two different approaches,
 501 both models are able to reproduce the lengthening of the starved dunes as observed in a laboratory
 502 flume (Figure 6).

503 The key findings of our modelling study also agree with existing field measurements of starved
 504 fluvial dunes. Kleinhans et al. (2002) described the observations and measurements of several
 505 type of bedforms in the gravel-bed river Allier (Moulis, France) over a period of low flow during
 506 which the river bed was fully armoured. Sand wave fields of fine sand ($d_s \simeq 0 \div 5$ mm), the area of

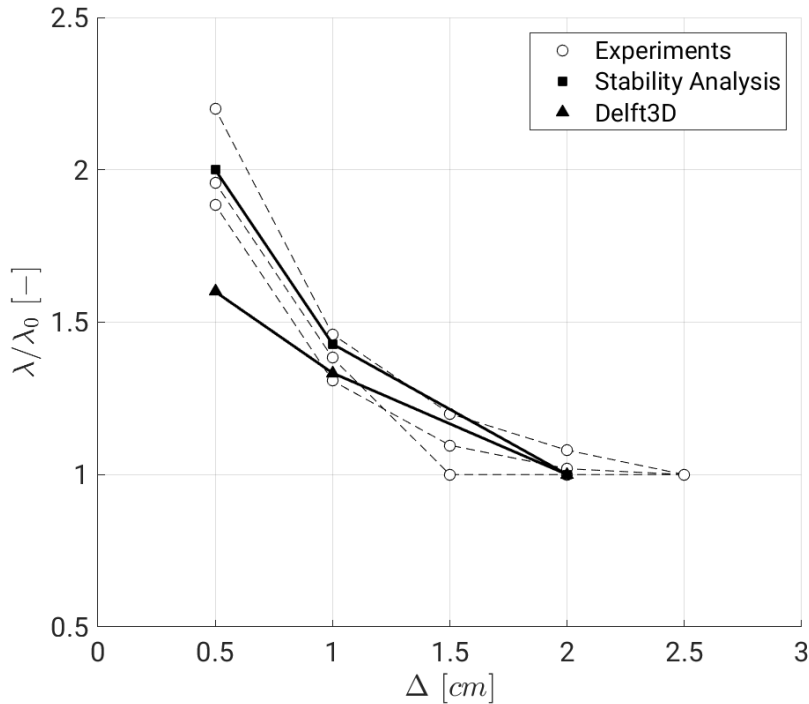


Figure 6: Comparisons of modelling outcomes with experimental measurements of the lengthening of starved dunes. Values of starved dune crest-to-crest distances are normalised by the wavelength of alluvial dunes observed for the same hydrodynamic and morphodynamic parameters and then plotted versus the thickness Δ^* of the sand layer initially available for transport.

507 which ranges from few squared metres to few hundreds of metres, were found to migrate over the
508 armour layer (85% gravel, $d_s \simeq 18$ mm) as a result of bank erosion and detachment of sand from
509 meander pools. These sand waves provided a spatially varying supply of mobile sediment for the
510 formation of bedforms in equal hydrodynamic conditions and sediment parameters. Regularly
511 spaced transverse dunes appeared in the inner part of these sand deposits, where the thickness
512 of the sand coverage attains its maximum value. Then, these bedforms gradually changed in
513 both the upstream and the downstream directions resulting into amorphous bedforms with more
514 sinuous crests. At the front and rear edge of each sand wave field, the armour layer was fully
515 exposed and amorphous dunes concurrently with sand ribbons were observed. Analogously to
516 our model results, the field observations of Kleinhans et al. (2002) suggest that the main factor
517 in determining the geometric characteristics of the emerging bedforms is the thickness of the
518 layer of sediment available for transport. The gradual transition from regular alluvial dunes to
519 irregular starved dunes is the same as that observed in the present study.

520 Similar starved patterns were observed by Carling et al. (2000b) in a supply limited reach of
521 the river Rhine (Mainz, Germany). Carling et al. (2000b) report the presence well sorted medium
522 sand ($d_s \equiv 0.9$ mm) in the form of different morphological patterns migrating over gravel lags
523 mainly composed of pebbles and cobbles ($d_s \simeq 10$ mm). Two distinct populations of bedforms
524 were identified: two-dimensional small dunes ($\lambda \simeq 1 \div 5$ m) with relatively straight crest, which
525 were roughly transverse to the primary flow direction, and three-dimensional large dunes ($\lambda \simeq$
526 $20 \div 50$ m) with either amorphous or barchanoid planforms. Carling et al. (2000b) described
527 in detail two large isolated dunes preceded by smaller starved dunes with crest-to-crest distance
528 approximately equal to 2 m. These smaller dunes were found to migrate over the stoss side of the
529 larger bedforms while decreasing in length ($\lambda \leq 1$ m). Further downstream they appear to have
530 generally grown in dimensions ($\lambda \geq 2$ m) across the gentle stoss side of the parent dune up to the
531 crestral region, where their transition to upper-stage plane bed was observed. Proceeding further
532 downstream, the smaller dunes often reformed increasing in length migrating over the intervening
533 gravel lags. All that being said, these field observations seem to indicate that sediment starvation
534 manifests itself by forming static isolated large dunes as well as by affecting the dimensions of
535 migrating small dunes. Particularly, the lengthening of the small dunes as they migrate from the
536 gentle lee side of isolated barchan dunes to the gravel lags is consistent with the lengthening of
537 the starved dunes predicted by our models.

538 Conversely, flume experiments designed to study the effects of sediment starvation on dune
539 growth have led to contradictory results. The experiments of Kleinhans et al. (2002) and Venditti
540 et al. (2019) identified a sequence of emerging bedforms in steady currents and the profile of these
541 bedforms was observed to depend on the sediment available for transport. Differently with the
542 experiments we used for our model validation, they provided sediment from upstream, observing
543 the gradual growth of different kind of bedforms. As the sediment supply increased, Kleinhans
544 et al. (2002) found a transition from sand ribbons to irregular sandy mounds and finally two-
545 dimensional trasverse dunes. Despite a clear indication on the dimensions of starved dunes

546 with respect their alluvial counterparts was not provided, their findings seem qualitatively in
547 agreement with our modelling results.

548 Differently, the experiments of Tuijnder et al. (2009) show dune geometries that progressively
549 decrease in size as the availability of mobile sediment decreases and the immobile coarser un-
550 derlayer is bared by the growth of the dunes. Among the several possible explanations to the
551 contradiction between these observations and our results (see Porcile et al., 2020 for an extensive
552 discussion), we believe the difference in the sediment and the associated skin roughness to be
553 crucial. Tuijnder et al. (2009) employed two different grain sizes for the immobile substrate and
554 the mobile layer. The coarser grain size of the substrate was selected to be immobile under the
555 action of the forcing flow. As a consequence, the exposition of the substrate led not only to sedi-
556 ment starvation, but also to a discontinuity in skin bottom roughness. Conversely, our numerical
557 modelling and the experiments used for its validation assume a substrate roughness which is
558 the same as the skin roughness representing the one single grain size available for transport.
559 Both models used in this study would require additional developments to include the effects of
560 nonlinearities due to discontinuities in the bottom roughness.

561 Furthermore, a striking difference between both approaches is the predicted dune shape.
562 It can be seen that the linearised model predicts purely sinusoidal shapes, whereas the fully
563 nonlinear model predicts non-sinusoidal, asymmetric shapes. Comparing this bottom profile
564 with the triangular-shaped dunes observed in the laboratory experiments, this clearly confirms
565 the general idea that strong nonlinearities imply asymmetric dunes.

566 Less information is available in the literature on the effect that sediment starvation has on
567 the migration of bedforms. The experimental measurements reproduced by our modelling results
568 cannot reveal useful information on starved dunes migration as they were conducted without re-
569 circulation of the sediment and thus limited in time (the experiments lasted only 30 minutes.
570 Thus, future experimental and modelling studies are required to properly investigate the effects
571 that the lack of mobile sediment has on bedform migration. Finally, in order to place this work
572 within a broader field of research, the (2DV) hydrodynamic model could be straightforwardly ex-
573 tended in the third direction. There is a body of work that shows that eolian dune size and spacing
574 is the result of finite-amplitude interactions and how these interactions can cause the lengthening of
575 desert barchan dunes (Hersen et al., 2004; Worman et al., 2013; Khosronejad and Sotiropoulos,
576 2017). However, an extension of the present modelling to account for three-dimensional effects
577 could be used for discussing subaqueous barchan dunes as a prominent example of dunes in a
578 sediment-limited environment, rather than necessarily reflecting only finite-amplitude interac-
579 tions. Moreover, the fully nonlinear Delft3D model is currently also used to study sediment
580 starvation in tidal sand waves (Damveld et al., 2021). Hopefully, the flow module of the model
581 could also be extended to study the atmospheric boundary layer making the present stability
582 analysis able to investigate the effects of sediment starvation on the morphology of eolian sandy
583 patterns.

584 6 Conclusions

585 In this study two different process-based modelling techniques have been applied to investigate
586 the genesis of fluvial dunes in case of sediment starvation. Previous laboratory experiments of
587 Porcile et al. (2020) have been used to provide controlled empirical foundations for the development
588 of process-based idealised models able to reproduce the effects that sediment starvation has on
589 the growth of these bedforms. An hypothesis has been formulated which states that the lack of
590 sand affects sediment transport and, in turn, bedform pattern, when a motionless substratum
591 is exposed by the formation of fluvial dunes. This hypothesis has then been tested by means
592 of numerical simulations in the framework of the stability analysis of a sandy bottom forced by
593 steady currents as well as the fully numerical modelling of its time development.

594 Generally, the laboratory measurements indicate that the exposition of the rigid bottom
595 strongly affects the characteristics of the emerging dunes, whose spacing increases and become
596 more irregular with a decreasing initial sediment availability. In line with these experimental
597 findings, simulations of the short-term time-development of small-amplitude dunes performed by
598 means of the stability-based model predict starved dunes with longer crest-to-crest distances than
599 those of alluvial dunes for the same values of hydrodynamic and morphodynamic parameters.
600 Finally, similar modelling outcome has been obtained by the finite-amplitude model confirming
601 the lengthening of starved fluvial dunes. Differently from the stability analysis, this fully numer-
602 ical model is able to reproduce final bottom configurations whose profile is even closer to that
603 observed during laboratory experiments, as it accounts for nonlinear effects other than sediment
604 starvation. This paves the way to the modelling of field-scale starved dunes and to potentially
605 deal with the long-term dynamics of these patterns to describe their equilibrium geometry and
606 migration. Also, an extension of our modelling exercise would allow to include further nonlin-
607 ear mechanisms that have been neglected so far, such as those associated with gravity, bottom
608 roughness, sediment sorting and three-dimensional flow and sediment transport.

609 7 Data Availability Statement

610 Datasets for this research are included in the following paper (and its supplementary information
611 files): Porcile, G., Blondeaux, P. and Colombini, M. 2020. Starved versus alluvial river bedforms:
612 an experimental investigation, *Earth Surface Processes and Landforms*, vol. 45 (5), pp. 1229-
613 1239, <https://doi.org/10.1002/esp.4800>.

614 References

- 615 J. Allen. The nature and origin of bed-form hierarchies. *Sedimentology*, 10(3):161–182, 1968.
- 616 P. Blondeaux, G. Vittori, and M. Mazzuoli. Pattern formation in a thin layer of sediment. *Marine*
617 *Geology*, 376:39–50, 2016.

- 618 P. Carling, E. Golz, H. Orr, and A. Radecki-Pawlik. The morphodynamics of fluvial sand dunes
619 in the River Rhine, near Mainz, Germany. I. Sedimentology and morphology. Sedimentology,
620 47(1):227–252, 2000a.
- 621 P. Carling, J. Williams, E. Golz, and A. Kelsey. The morphodynamics of fluvial sand dunes
622 in the River Rhine, near Mainz, Germany. II. Hydrodynamics and sediment transport.
623 Sedimentology, 47(1):253, 2000b.
- 624 M. Colombini. Revisiting the linear theory of sand dune formation. Journal of Fluid Mechanics,
625 502:1–16, 2004.
- 626 M. Colombini and A. Stocchino. Finite-amplitude river dunes. Journal of Fluid Mechanics, 611:
627 283–306, 2008.
- 628 M. Colombini and A. Stocchino. Ripple and dune formation in rivers. Journal of Fluid Mechanics,
629 673:121, 2011.
- 630 M. Colombini and A. Stocchino. Three-dimensional river bed forms. Journal of Fluid Mechanics,
631 695:63–80, 2012.
- 632 J. H. Damveld, B. W. Borsje, P. C. Roos, and S. J. M. H. Hulscher. Hor-
633 izontal and vertical sediment sorting in tidal sand waves: Modeling the finite-
634 amplitude stage. Journal of Geophysical Research: Earth Surface, 125(10):
635 e2019JF005430, 2020. ISSN 2169-9003. doi: 10.1029/2019JF005430. URL
636 <https://agupubs.onlinelibrary.wiley.com/doi/abs/10.1029/2019JF005430>.
- 637 J. H. Damveld, G. Porcile, P. Blondeaux, and P. C. Roos. Nonlinear dynamics of sand waves in
638 sediment scarce environments. In EGU General Assembly 2021, 2021. doi: 10.5194/egusphere-
639 egu21-16019.
- 640 F. Engelund. Instability of erodible beds. Journal of Fluid Mechanics, 42(2):225–244, 1970.
- 641 F. Engelund and J. Fredsoe. Sediment ripples and dunes. Annual Review of Fluid Mechanics,
642 14(1):13–37, 1982.
- 643 R. Fernandez Luque and R. Van Beek. Erosion and transport of bed-load sediment. Journal of
644 hydraulic research, 14(2):127–144, 1976.
- 645 J. Fredsøe. On the development of dunes in erodible channels. Journal of Fluid Mechanics, 64
646 (1):1–16, 1974.
- 647 J. Fredsøe and R. Deigaard. Mechanics of coastal sediment transport, volume 3. World scientific,
648 1992.
- 649 H. P. Guy, D. B. Simons, and E. V. Richardson. Summary of alluvial channel data from flume
650 experiments, 1956-61. US Government Printing Office, 1966.

- 651 P. Hersen, K. H. Andersen, H. Elbelrhiti, B. Andreotti, P. Claudin, and S. Douady. Corridors of
652 barchan dunes: Stability and size selection. Physical Review E, 69(1):011304, 2004.
- 653 J. F. Kennedy. The formation of sediment ripples, dunes, and antidunes. Annual review of fluid
654 mechanics, 1(1):147–168, 1969.
- 655 A. Khosronejad and F. Sotiropoulos. On the genesis and evolution of barchan dunes: morpho-
656 dynamics. Journal of Fluid Mechanics, 815:117–148, 2017.
- 657 M. Kleinhans, A. Wilbers, A. De Swaaf, and J. Van Den Berg. Sediment supply-limited bedforms
658 in sand-gravel bed rivers. Journal of sedimentary research, 72(5):629–640, 2002.
- 659 G. R. Lesser, J. A. Roelvink, J. A. T. M. van Kester, and G. S. Stelling. Develop-
660 ment and validation of a three-dimensional morphological model. Coastal Engineering,
661 51(8–9):883–915, 2004. ISSN 0378-3839. doi: 10.1016/j.coastaleng.2004.07.014. URL
662 <http://www.sciencedirect.com/science/article/pii/S0378383904000870>.
- 663 G. Parker, P. C. Klingeman, and D. G. McLean. Bedload and size distribution in paved gravel-
664 bed streams. Journal of the Hydraulics Division, 108(4):544–571, 1982.
- 665 G. Porcile, P. Blondeaux, and G. Vittori. On the formation of periodic sandy mounds.
666 Continental Shelf Research, 145:68–79, 2017.
- 667 G. Porcile, P. Blondeaux, and M. Colombini. Starved versus alluvial river bedforms: an experi-
668 mental investigation. Earth Surface Processes and Landforms, 45(5):1229–1239, 2020.
- 669 A. Reynolds. A decade’s investigation of the stability of erodible stream beds. Hydrology
670 Research, 7(3):161–180, 1976.
- 671 K. J. Richards. The formation of ripples and dunes on an erodible bed. Journal of Fluid
672 Mechanics, 99(3):597–618, 1980.
- 673 G. Seminara. Fluvial sedimentary patterns. Annual Review of Fluid Mechanics, 42:43–66, 2010.
- 674 A. P. Tuijnder, J. S. Ribberink, and S. J. Hulscher. An experimental study into the geometry of
675 supply-limited dunes. Sedimentology, 56(6):1713–1727, 2009.
- 676 V. A. Vanoni and N. H. Brooks. Laboratory studies of the roughness and suspended load of
677 alluvial streams. US Army Engineer Division, Missouri River, 1957.
- 678 J. G. Venditti, P. A. Nelson, R. W. Bradley, D. Haught, and A. B. Gitto. Bedforms, structures,
679 patches, and sediment supply in gravel-bed rivers. Gravel-Bed Rivers: Process and Disasters,
680 439, 2017.
- 681 J. G. Venditti, J. A. Nittrouer, M. A. Allison, R. P. Humphries, and M. Church. Supply-limited
682 bedform patterns and scaling downstream of a gravel–sand transition. Sedimentology, 66(6):
683 2538–2556, 2019.

684 S. L. Worman, A. B. Murray, R. Littlewood, B. Andreotti, and P. Claudin. Modeling emergent
685 large-scale structures of barchan dune fields. Geology, 41(10):1059–1062, 2013.